



This is a repository copy of *Image feature delocalization in defocused probe electron ptychography*.

White Rose Research Online URL for this paper:
<http://eprints.whiterose.ac.uk/126696/>

Version: Accepted Version

Article:

Cao, S., Maiden, A. and Rodenburg, J.M. orcid.org/0000-0002-1059-8179 (2018) Image feature delocalization in defocused probe electron ptychography. *Ultramicroscopy*, 187. pp. 71-83. ISSN 0304-3991

<https://doi.org/10.1016/j.ultramic.2018.01.006>

Reuse

This article is distributed under the terms of the Creative Commons Attribution-NonCommercial-NoDerivs (CC BY-NC-ND) licence. This licence only allows you to download this work and share it with others as long as you credit the authors, but you can't change the article in any way or use it commercially. More information and the full terms of the licence here: <https://creativecommons.org/licenses/>

Takedown

If you consider content in White Rose Research Online to be in breach of UK law, please notify us by emailing eprints@whiterose.ac.uk including the URL of the record and the reason for the withdrawal request.



eprints@whiterose.ac.uk
<https://eprints.whiterose.ac.uk/>

Image feature delocalization in defocused probe electron ptychography

S. Cao*, A.M. Maiden and J.M. Rodenburg

*Department of Electronic and Electrical Engineering, University of Sheffield, Sheffield S1
3JD, United Kingdom*

**Corresponding author: now affiliated to the Institute of Physics, Humboldt University
Berlin, Newtonstr. 15, 12489, Berlin, Germany.*

Abstract

Electron ptychography can in principle convert a conventional scanning electron microscope (SEM) into a good quality transmission electron microscope (TEM). An improvement in resolution of about a factor of 5 over the lens-defined resolution of an SEM was first demonstrated in 2012 by Humphry et.al. However, the results from that work showed some delocalization in the atomic fringes of the gold particles used as a test specimen for the technique. Here we explore factors that result in the delocalization effect when a defocused probe is used for the ptychographic data collection: source incoherence, the effects of detector faults, data truncation and a poorly calibrated illumination step size (or camera length). Various mitigation strategies are tested, including modal decomposition of the incoherence in the beam. We reprocess the data from the original SEM experiment to show that these refinements significantly improve the reconstruction.

1 Introduction

There are a number of different optical configurations possible for electron ptychography. In its original form, a lens was used to focus a diffraction-limited spot (a probe) into the plane of the specimen, with diffraction data being recorded on a two-dimensional pixelated detector in the Fraunhofer plane far downstream from the object. In order to satisfy the overlap requirement (1), the probe must be scanned on a very fine grid, with two-dimensional diffraction patterns being recorded from every pixel required for the final reconstruction. Two closed form inversion methods for this type of data, which is densely sampled in real-space, were developed during the 1990s. A real-space inversion method, called Wigner Distribution Deconvolution (WDD) (2), can be used if the illumination has sharp features in it (never the case for a probe propagated from another plane in the microscope). In practice, in the scanning transmission (STEM) mode, a reciprocal version of WDD must be employed (3), which also has the advantage of allowing partial spatial coherence effects to be removed from the data. A second closed form method can apply when the object is weakly scattering, in which case the deconvolution is not necessary (4). A much simplified approach can be employed if the object is crystalline (5): a configuration that most closely resembles Hoppe's original proposal for ptychography (6) (7), but which cannot practically be applied to general objects. All these methods were in those days greatly hampered by poor detector technology and the small computer memory available. There is now renewed interest in this type of ptychography: recent results using the latest detector technology have proved very successful [8 - 11]. However, the data size demands are still phenomenal: these techniques require a whole diffraction pattern to be recorded for each of the pixels in the final reconstruction.

The recent widespread adoption of ptychography in the X-ray community arose from the advent of iterative ptychographic reconstruction techniques [12 - 17]. This approach has the advantage of imaging an extended area of the object, moving a large patch of illumination in

large steps: i.e. the sampling in real space can be made coarse [13]. One of the benefits of this approach is speed, because a large field of view can be spanned very quickly. There is also a much smaller requirement on the amount of data that needs to be collected and stored.

Furthermore, unlike in the focused probe configuration, the lens used to condense the electrons can have a small angular size if the principal source of high-resolution information arises from the dark-field region of the diffraction pattern lying outside the bright central Ronchigram.

A possible application for this type of large probe electron ptychography is to convert a machine of moderate specification, such as a conventional scanning electron microscope (SEM), into a good quality transmission electron microscope (TEM) simply by placing a two-dimensional detector behind a specimen holder that can accommodate a transmission specimen. A proof-of-principle of this approach was demonstrated some years ago [19].

However, the community expressed some doubt about the results, specifically that the fringes in the gold particles used as a test specimen were, in some instances, delocalized, extending beyond the boundaries of the particles.

In the present work, we investigate various influences that affect the fidelity of electron ptychographic reconstructions in this defocused probe configuration, especially as they relate to delocalization of atomic fringes. Clearly, if fringes (i.e. Fourier components comprising the image) are laterally shifted, which is equivalent to their diffracted intensities being assigned the wrong phase, then the image is meaningless as far as interpreting the position of atomic columns, rather like an out of focus conventional bright-field image that has negative regions in its contrast transfer function. We test here via model calculations the effects of 1) partial spatial coherence caused by the source size, 2) a noise pedestal in the detector output, 3) the point spread function of the detector, 4) abrupt truncation of the signal at the detector edges, and 5) errors in the probe positions. We then examine the efficacy of various methods for

removing these imperfections in the data via simulation, before applying the same methods to the experimental SEM data used for the results reported by Humphry et. al. [19].

It should be noted that X-ray ptychography is often undertaken with a defocused probe, formed either by Kirkpatrick-Baez mirrors or a Fresnel Zone plate lens (for example [20]). By shifting the object up and downstream of the plane of the focused beam, the illumination size can be conveniently altered to match the field of view required in the experiment, especially in relation to the data size limitations and the time taken for a large scan. However, the sort of problems we describe here very rarely impact on the X-ray configuration. First, the detectors used (certainly at hard X-ray energies) are single photon counting and effectively perfect. Second, the optical configuration in the beamline of a third generation synchrotron beamline results in a more coherent wavefield than that generated by a Schottky FEG source in a typical SEM, given typical condenser lens excitations in SEM. Thirdly, the exact defocus, step size and object to camera distance can be measured explicitly and very accurately, avoiding the scan scaling problem we will describe below.

2 Factors affecting delocalization of reconstruction features

In this section we undertake a series of model calculations to indicate the effects of various imperfections in defocused probe ptychography data. The physical scale of our model is irrelevant, except insofar as the relative size of the component elements of the experiment are realistic. For the sake of definiteness, we model atomic fringes in gold, separated by 0.204nm, as in Fig. 2, and scale the probe size, source size, defocus and detector size to be consistent with a SEM. We do not model Poisson noise (shot noise) in the data, and so the detected intensities described in Section 2.3 are arbitrary, although the relative size of the signal verses read-out pedestal, etc., is representative of a real detector.

2.1 Source transverse partial coherence

In the previous reconstruction of the data collected on the SEM [19], the illumination was assumed to be fully coherent, which means the source was assumed to be a point source. In reality, the source of an electron microscope is never fully coherent [21 - 24]. The source generated by a field emission gun has a physical size of about 10nm [18], which can be demagnified into a beam spot of several angstroms by the condenser lenses and condenser aperture. Fig. 1.a shows a simulated symmetric source with a dimension of about 25\AA^2 , as focused in the specimen plane. It was modelled by a two-dimensional Gaussian function, with an arbitrary maximum value of 1. Values below 0.2 were put to 0 to suppress the unphysical effects of the Gaussian's indefinite extent. The incoherent illumination formed with this source at a defocused plane is shown in Fig. 1.b, which was simulated by propagating each point source to the Fourier domain, multiplying with an aperture, propagating to the defocused plane, and superposing the illuminations formed from each point source. In other words, the probe formed from one point on the source is

$$P_a = \mathcal{F}^{-1}\{\mathcal{F}\{S_a\} \times A \times e^{i\phi}\}, \quad (1)$$

and the incoherent illumination is given by

$$P_{incoherent} = \sum_{a=1}^m |P_a|^2. \quad (2)$$

where \mathcal{F} represents the Fourier transform, S_a represents the a^{th} point source in the source plane, A represents the condenser aperture, and $e^{i\phi}$ is the phase change introduced by aberrations in the lens. All these variables are functions of two-dimensional coordinates, which, for simplicity, we do not include.

When the partially coherent illumination is transmitted through an object, the diffraction pattern intensities on the detector are

$$I_{pc} = \sum_{a=1}^m |\mathcal{F}\{P_a \times O\}|^2, \quad (3)$$

where I_{pc} is the partially coherent diffraction pattern, and O is the object.

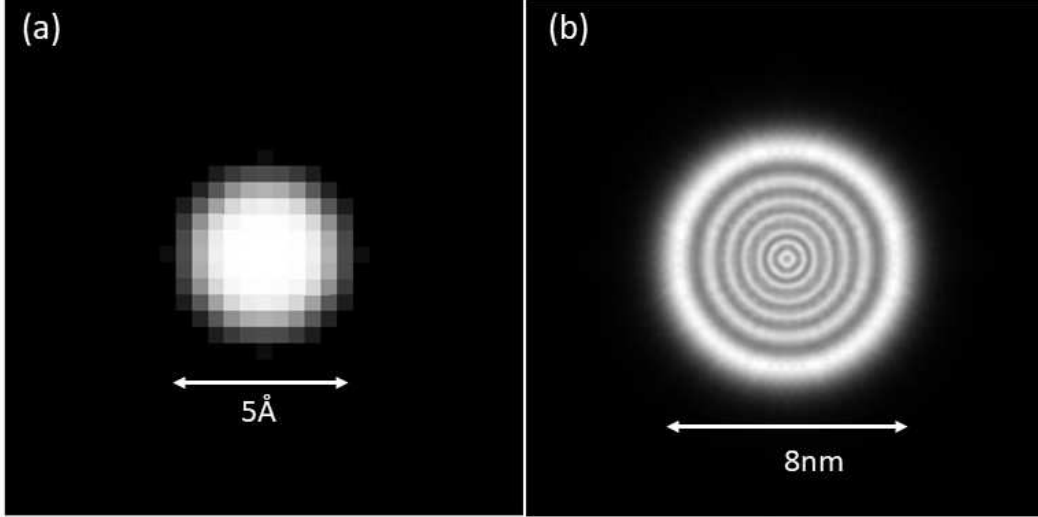


Fig. 1. (a) is the transverse partially coherent source used for the simulations; the dimension of the source is about $5\text{Å} \times 5\text{Å}$. (b) shows the partially coherent illumination generated from (a) according to the setup shown in Fig. 3; this is the illumination used to simulated the partially coherent diffraction patterns for the ptychographic reconstruction.

Fig. 2 shows the object used for the simulations in this paper. It is a complex object, with the modulus varying between 0 and 1 and the phase varying between -1 and 1. The fringes mimic the fringes of the atomic layers in the gold particles in the real experiment we look at in Section 3. The red crosses on the object show the probe scanning positions when collecting the ptychographic data, and the circle shows roughly the size of the probe. Fig. 3 shows the experimental setup for the simulations. In all that follows, we will only show the phase of the reconstructions we obtain under various processing conditions. We have found that the data flaws we examine only affect structural information (fringe positions etc.): features in the modulus reconstructions are broadly identical to those in the phase reconstructions.

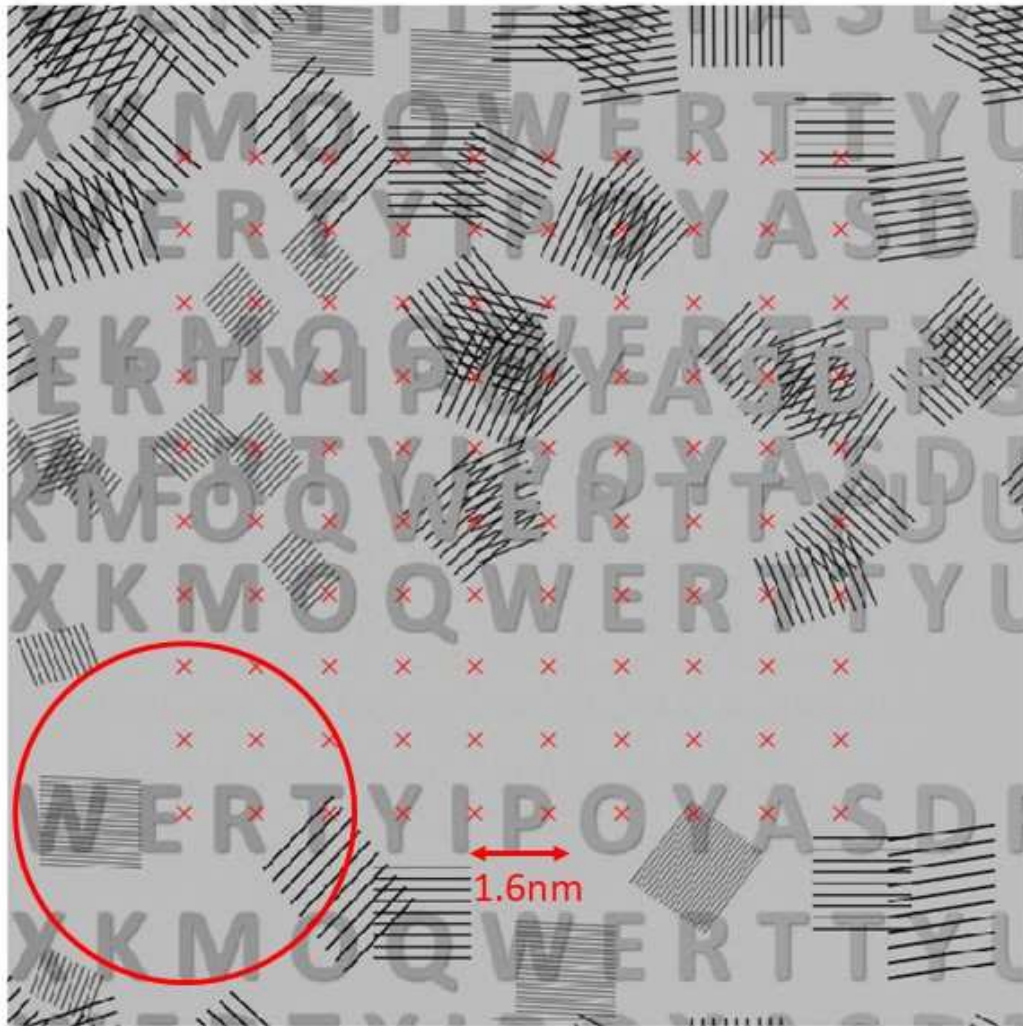


Fig. 2 shows the modulus of the complex object used the simulations. The modulus of the object varies between $[0, 1]$; the phase of the object is the same pattern with the modulus, varying $[-1, 1]$. The red crosses show the scanning positions when collecting the ptychographic data. The red circle shows roughly the size of the probe.

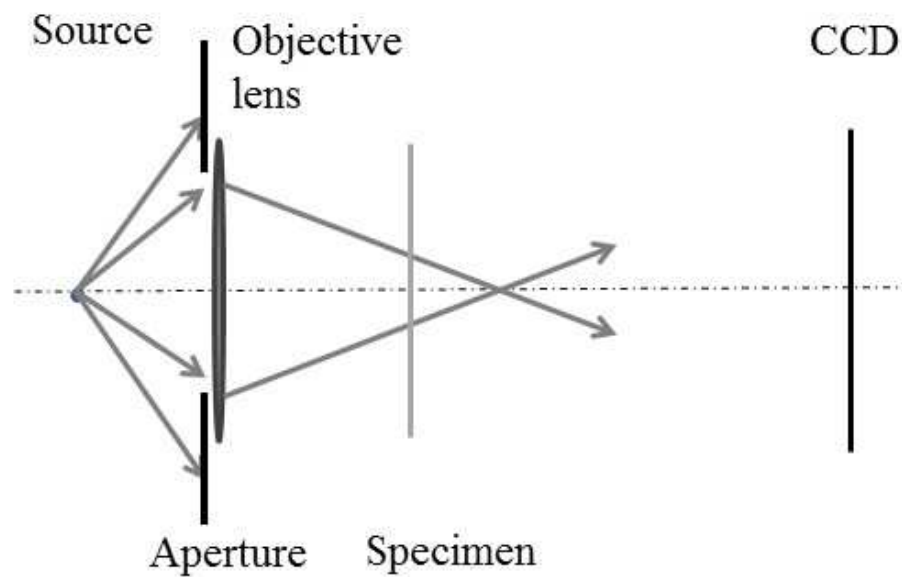


Fig. 3 shows the setup engaged for the simulations, which is also a simplified configuration of the experimental setup: a condenser aperture was inserted in the far field with respect to the source domain; the objective lens formed a probe at a slightly defocused plane on the specimen; the detector was placed in the far field respect to the sample.

Fig. 4 compares the diffraction patterns generated from coherent illumination and the partially coherent illumination shown in Fig. 1.b. We can see that, when the illumination is fully coherent, the diffracted structures inside the central disk of the Ronchigram have clear fringes, which are related to the structure of the sample. When the illumination is partially coherent, the diffracted fringes inside the central disk of the Ronchigram are blurred. Fig. 5.a shows the ptychographic reconstruction from the partially coherent data with the conventional ePIE algorithm [17], assuming the illumination is fully coherent. The reconstruction quality is poor: object features are blurred and moreover the fringes are indeed delocalized. This suggests that source transverse partial coherence is one cause of fringe delocalization in the original SEM experiment.

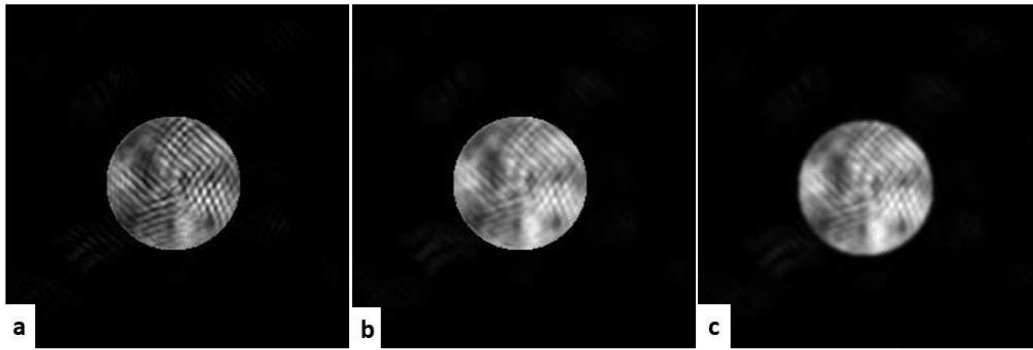


Fig. 4 shows the examples of the diffraction patterns generated from (a) fully coherent illumination and (b) partially coherent illumination. (c) shows one diffraction pattern generated from coherent illumination, while considering the point spread function of the detector; the detector point spread function was approximated as a 2-dimensional Gaussian profile with the derivation of 1.5 pixels in both dimensions. The aperture size is 12mrad.

There are two methods for removing the effects of partial coherence in ptychographic reconstructions: Gaussian blind convolution [22 - 23] and modal decomposition [18] [25 - 27]. The former assumes the source has the effect of blurring the diffraction pattern. This is strictly only true if the object lies in the Fraunhofer plane of the source and the detector lies in the Fraunhofer plane of the object, so that in the absence of a specimen, the detector plane records an image of the source distribution. In the STEM-type configuration we have here, the specimen (not the detector) lies in the plane of the image of the source. In fact, with a defocused illumination these extreme situations become mixed up with one another because the Ronchigram is a Fresnel image of the object.

The most effective approach is therefore to use a modal decomposition of the source partial coherence. Instead of having a single, pure state model of illumination (as would arise from a perfect point source), the wavefield is represented by a number of states (waves), each of which is entirely incoherent with respect to the other states, but coherent within themselves, and hence can be propagated through the experiment independently. Here we apply the modal decomposition method based on the ePIE algorithm. Instead of engaging a single

illumination function as in the conventional ePIE reconstruction, we use six independent illumination profiles. Thus, in the Fourier domain, the update function at each scanning position becomes

$$\Psi'_n = \sqrt{I} \frac{\Psi_n}{\sqrt{\sum_n |\Psi_n|^2}}, \quad (4)$$

where n labels the order of each probe function, I is the detected intensity, and Ψ_n is the Fourier transform of the n th exit wave. (As before, we omit spatial coordinates for these functions.)

We propagate each Ψ'_n to real space by a Fourier transform, to get the updated exit wave functions ψ'_n . The next step is to update each of the probe functions and the object function by

$$P'_n = P_n + \alpha \frac{\psi'_n \cdot O^*}{|O|_{max}^2}, \quad (5)$$

$$O' = O + \beta \cdot \frac{\sum_n (\psi'_n \cdot P_n^*)}{\sum_n |P_n|^2}, \quad (6)$$

where P'_n is the n^{th} updated probe function, O^* is the conjugate of the object function, α and β are scaling factors to control the update step. Here we take $\alpha = 1$ and $\beta = 1$.

The specimen reconstruction of the partially coherent data resulting from the modal decomposition method is shown in Fig. 5.b., and compared with the conventional ePIE reconstruction (shown in Fig. 5.a). Fig. 7 shows the Fourier ring correlation (FRC) between the reconstruction results with the true object, which is nowadays the most common way of quantitatively characterising the quality of a ptychographic reconstruction. Clearly, the modal decomposition has greatly improved the quality of the reconstruction. In the image, the effect of the method is apparent: the features of the sample are clearer and the fringes are better localized. However, from the magnified features we can see that the fringes are still slightly

delocalized, which means that the effect of the source partial coherence has not been removed completely. As investigated in reference [25], the efficiency of the modal decomposition method is affected by 1) the specimen structure diversity, 2) the propagation distance, 3) the overlap amount in real space and 4) the reconstructed area. We infer that it is the specimen structure diversity affecting the modal decomposition reconstruction efficiency in this simulation. Fig. 6.a shows the reconstructed decompositions of the partially coherent illumination function at the sample plane. We use the most compact representation: the modes shown are all orthogonal to one another and derive from the diagonalized density matrix (see [25] for details). The values above each mode show the percentage of the corresponding mode contributes to the illumination function; the larger percentage the first mode has, the more coherent is the effective source. In this simulation, when the source size is about 5\AA , and the aperture size is 12mrad , the first mode takes about a 47% contribution of the illumination.

We can conclude that the transverse partial coherence of the source will result in the features delocalization in the ptychographic reconstruction (Fig. 5.a). Considering the coherence degree of the electron source of the SEM for collecting the data in the paper by Humphry et al. [19] source partial coherence is most likely one of the factors that result in feature delocalization. As has been demonstrated in the simulation data, modal decomposition is an effective method for removing the effects of partial coherence: it has improved the reconstruction quality significantly.

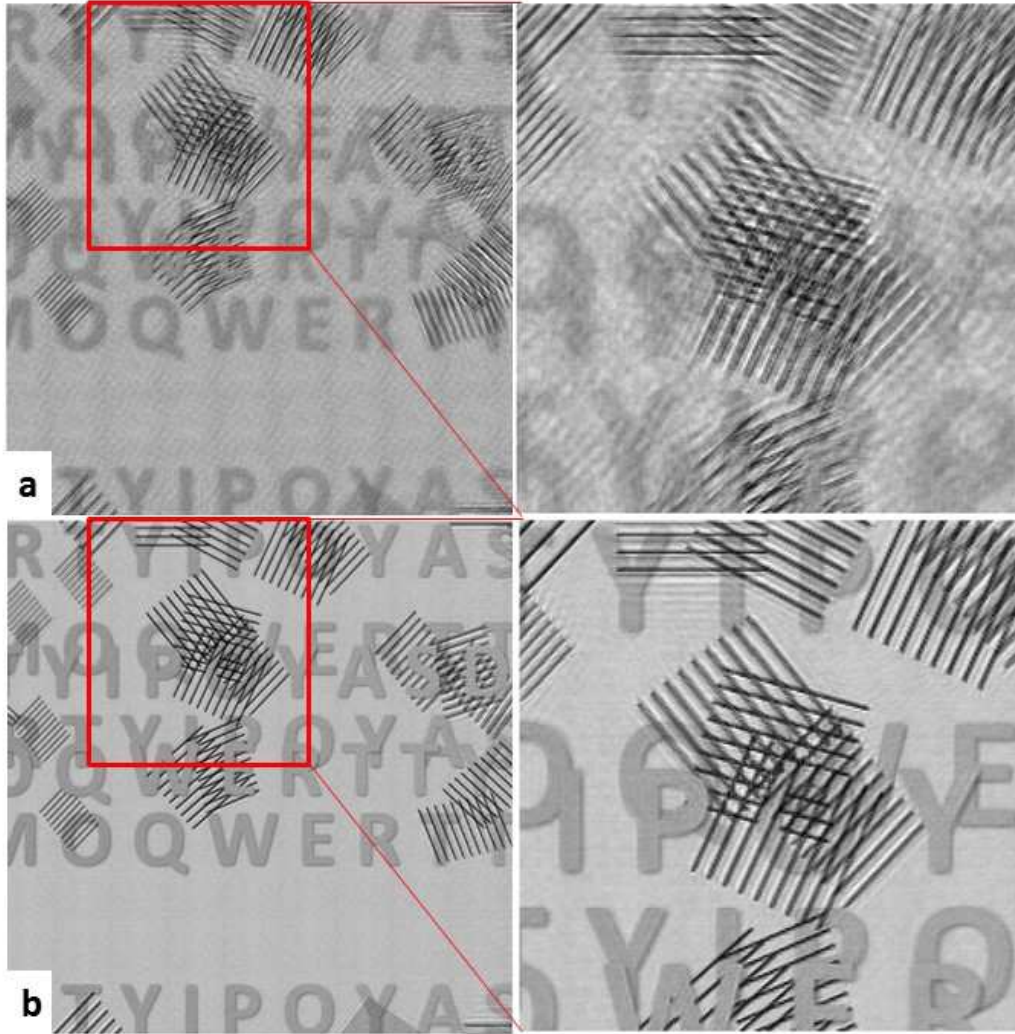


Fig. 5 compares the reconstructions from the partially coherent dataset with the conventional ePIE (a) and with the modal decomposition method (b). The figures on the right show the magnified features; we can see that when applying the conventional ePIE to reconstruct the partially coherent data, the reconstruction quality is poor; the features are unclear and delocalized; while the modal decomposition method has improved the reconstruction a lot, even though it has not completely removed the influence of the source partial coherence.

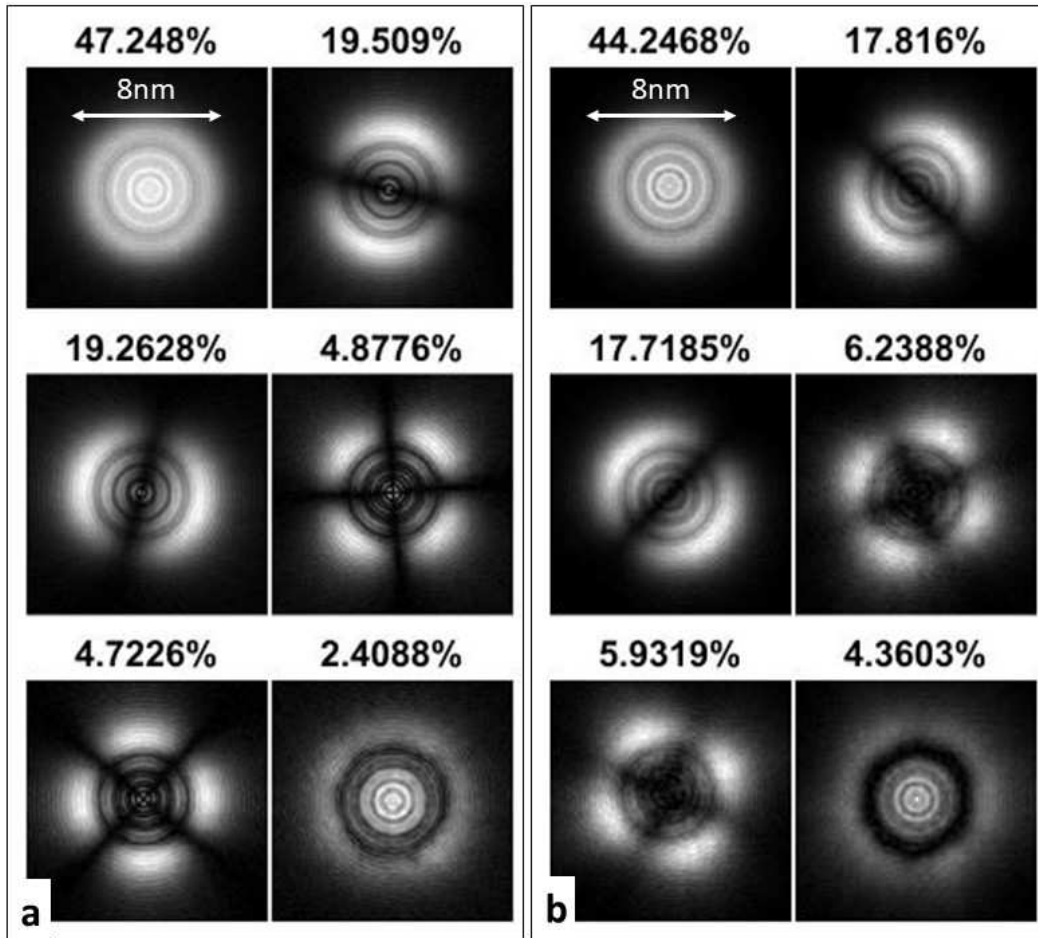


Fig. 6 shows the modes reconstructed with modal decomposition method at the sample plane. (a) shows the modes of the partially coherent source; the first mode takes about 47%. (b) shows the modes reconstructed from the data with the effect of detector point spread; the detector point spread was simulated as a Gaussian profile convolution with a standard derivation of 1.5 pixels; the first mode takes about 44%; the detector point spread has a similar effect with the source transverse partial coherence.

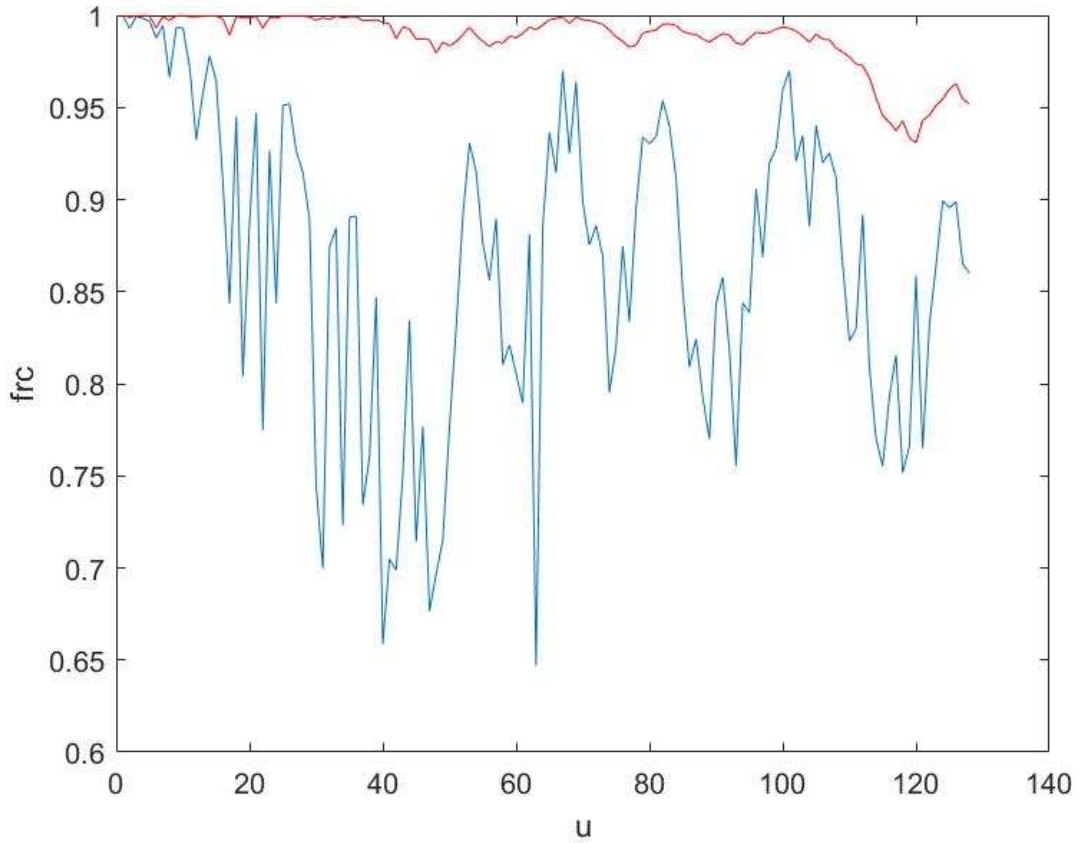


Fig. 7 plots the Fourier ring Correlation (FRC) of the reconstruction on the spatially partially coherent data. The blue line plots the FRC between the true object with the ePIE reconstruction; the red line plots the FRC between the true object with the modal decomposition reconstruction.

2.2 Detector point spread

The detector response property affects the quality of the diffraction pattern or the image directly. The experimental data in section 3 was collected using phosphor coupled via a fiber optic bundle to a CCD detector. Electrons incident on the phosphor spread out within it, causing a point spread function, blurring the diffraction pattern. We can model this approximately as a convolution of the true signal with a Gaussian profile, such that

$$I_{ps} = I \otimes G_{\sigma}, \quad (7)$$

where I_{ps} represents the diffraction pattern with the influence of detector point spread and G_σ is a Gaussian profile with standard deviation equals σ .

In the simulation, we generated a two-dimensional Gaussian profile with a standard deviation equal to 1.5 pixels, to simulate this effect. The reconstruction of the sample with the conventional ePIE algorithm is shown in Fig. 8.a. The reconstruction quality is similar to the result with the partially coherent data shown in Fig. 5.a: the features and the boundaries of the fringes are blurred. As demonstrated in previous work [18] [25], the modal decomposition method also works to remove the detector point spread effect on the specimen reconstruction, by retrieving the detector point spread as decomposed modes of the illumination. Fig. 8.b shows the reconstruction of the same data with the modal decomposition method. The features are clear and localized: the modal decomposition method has almost completely removed the effect of the detector point spread. Fig. 6.b shows the reconstructed modes from the data with the detector point spread effect. The modes have the same patterns as the modes reconstructed from the partially coherent data.

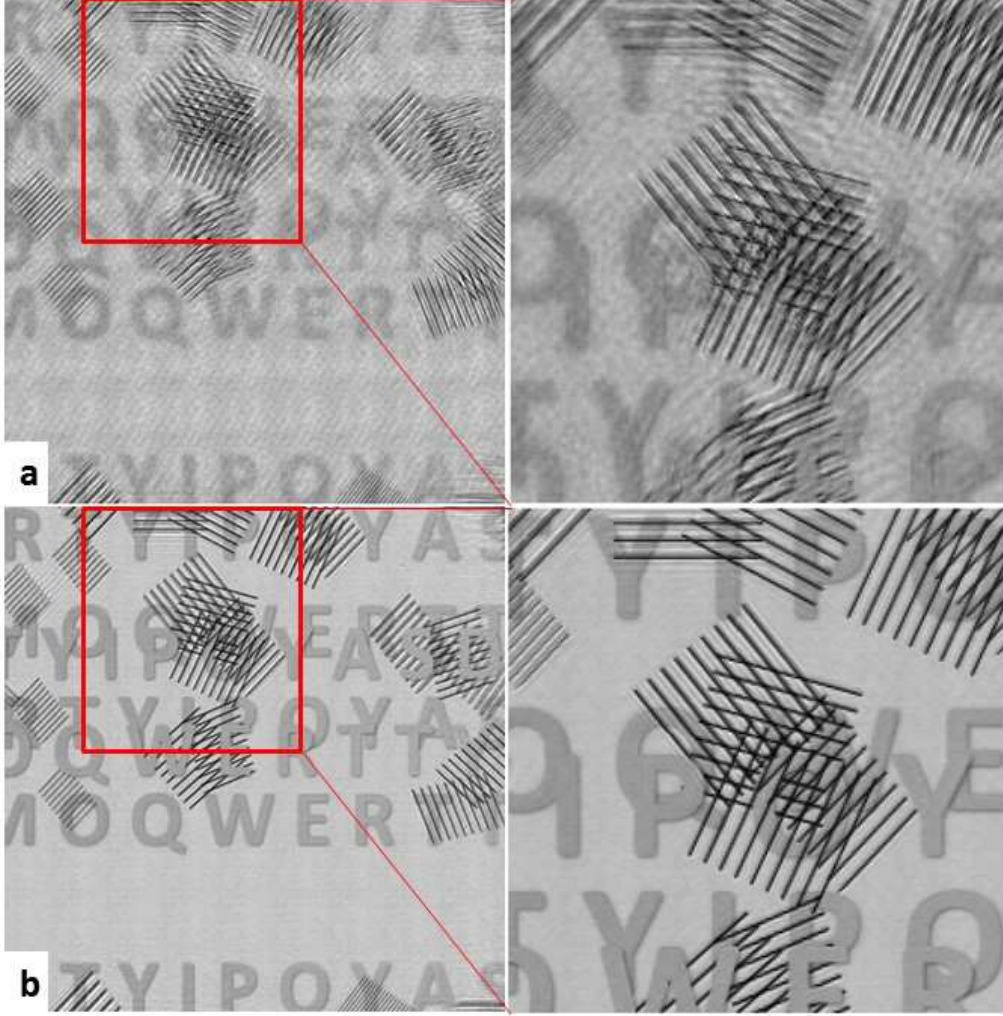


Fig. 8 shows the reconstructed phase from the data with the detector point spread effect. (a) is the reconstruction with the conventional ePIE algorithm; the features on the sample are blurred, and we cannot see the clear boundaries of fringes. (b) shows the reconstruction with the modal decomposition algorithm; the features and the boundaries are clear.

2.3 Detector pedestal

Another problem of the detector is the response pedestal, which may vary between pixels, and may change nonlinearly according to the strength of the excitation; thus, it will result in a distortion of the signal. We can characterize the response property of each pixel on the detector as

$$I_{out}(u) = I(u) + c(u), \quad (8)$$

where u denotes the pixels on the detector, and I_{out} denotes the readout value. $I(u)$ denotes the true signal while $c(u)$ denotes the pedestal at each pixel. Fig. 9 compares the diffraction pattern when adding constant pedestal, c , (which in this example is the same for all $c(u)$) of 0, 0.005, 0.01, and 0.5 on each pixel: absolute values are arbitrary, the average intensity in the central disc is 1.5 in this model calculation. We can see that, as the value of the pedestal increases, more high-frequency diffraction speckles disappear into the background. One ptychographic reconstruction with the conventional ePIE from the dataset when $c = 0.005$ is shown in Fig. 10.a: the reconstruction is very noisy, the features on the sample are blurred and some features, for example the letters in the background, have nearly disappeared.

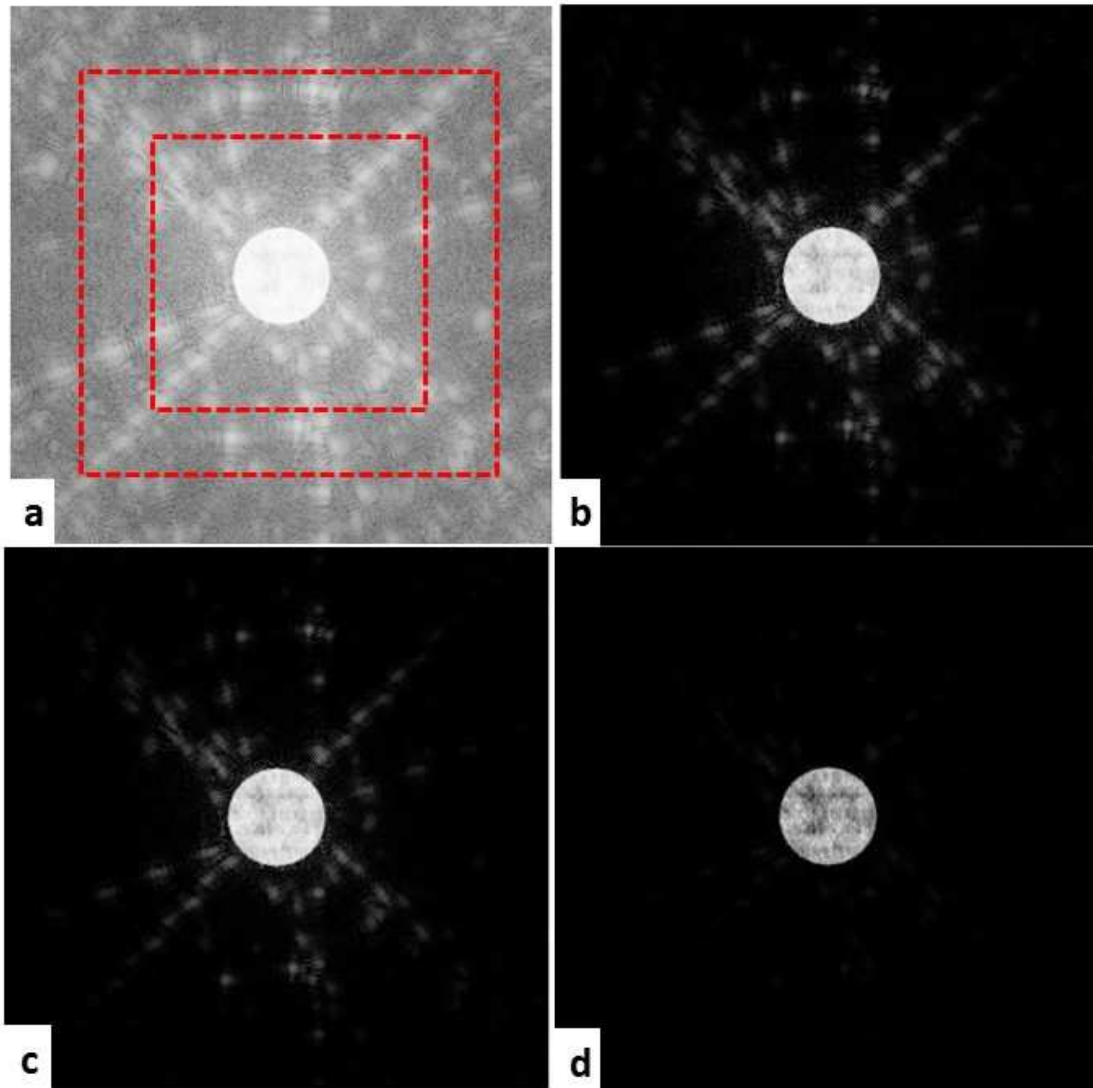


Fig. 9 shows the examples of the diffraction pattern when adding the response pedestal; the diffraction patterns are plotted in logarithm scale. (a) plots the clean diffraction pattern without pedestal; (b - d) plot the same diffraction pattern shown in (a) when adding constant pedestals of 0.005, 0.01 and 0.5. The pedestal obliterates some high-order diffraction speckles at the edge part of the pattern; as we increase the pedestal, more speckles disappear. The red dashed lines in (a) show the data reconstructed in the later section that was truncated by $\frac{1}{2}$ or $\frac{3}{4}$; the data truncation will also result in the loss of the high-order diffraction speckles.

One experimental way to reduce the influence of the detector pedestal is to remove a dark field reference from the image or diffraction pattern. The reference will be removed from

each diffraction pattern before processing. However, this method cannot remove the pedestal accurately because exposure of the phosphor can influence its sensitivity.

Several methods have been proposed to improve the ptychographic reconstruction with the pedestal data [22] [28 - 30]. In this paper, we compared the pedestal matching method and the extra mode method. Both of the methods try to work out the background $c(u)$ to match the calculated intensities I_c at each pixel with the detected intensities I_{out} ; the difference between arises from the method of updating $c(u)$. The pedestal matching method updates the $c(u)$ during the reconstruction, estimating $c(u)$ at each scanning position based on the error between the estimated and measured intensities, whilst the mode method essentially abandons any intensity that is not consistent with the single object constraint into a free mode that allows the forward calculation to be consistent with the measured data. The pedestal matching method updates the $c(u)$ at each scanning position by

$$c(j, u) = \gamma_j (I(j, u) - I_c(j, u)), \quad (9)$$

where j registers the probe positions, I_c is the calculated intensities, γ is the scaling factor update at each position given by

$$\gamma_j = \frac{\sum_u [I(j, u) * I_c(j, u)]}{\sum_u [I(j, u) * I(j, u)]}. \quad (10)$$

For the mode method, we use an extra probe function P_e and an extra object function O_e , to make the calculated intensities match the detected intensities such that

$$I = I_c + I_e, \quad (11)$$

where I_e is the intensity from the extra probe and extra object given by

$$I_e = |\mathcal{F}\{P_e \times O_e\}|^2. \quad (12)$$

At each position, we update the pedestal I_e by updating the extra object function and the extra probe function using

$$O'_e = O_e + \alpha \frac{P_e^*}{|P_e|^2} (\psi'_e - \psi_e), \quad (13)$$

$$P'_e = P_e + \beta \frac{O_e^*}{|O_e|^2} (\psi'_e - \psi_e) \quad (14)$$

This method essentially abandons any intensity that is not consistent with the single object constraint into a free mode that allows the forward calculation to be consistent with the measured data.

We retrieved the pedestal from the simulated data with both methods. Fig. 10.b shows the reconstruction when removing the pedestal with the extra mode method: Fig. 10.c shows the reconstruction when removing the pedestal with the pedestal matching method. Both of the reconstructions have been improved significantly; the features on the sample are clear, and the letters in the background are well reconstructed. Fig. 11 shows the reconstructed pedestal at one position from the extra mode method. The retrieved value of the pedestal outside the central disk is about 0.005, which is exactly the pedestal we added to the original diffraction patterns. However, in the central disk area, the algorithm failed to retrieve the pedestal inside the disk. The reason it resulted in this may be because the intensities of the diffraction pattern inside the central disk have an average value of 1.5, so when a pedestal of 0.005 is added it is 0.3% of the detected intensities, and so the algorithm is not sensitive enough to retrieve such a small error. Fig. 12 plots the FRCs of the reconstructions. We can see that both the extra mode method and the background matching method improve the reconstruction quality at high and low frequencies significantly.

We conclude that the pedestal of the detector will make the ptychographic reconstruction very noisy, and will decrease resolution. Both the pedestal matching method and the extra mode method can retrieve the pedestal accurately, and improve the reconstruction effectively.

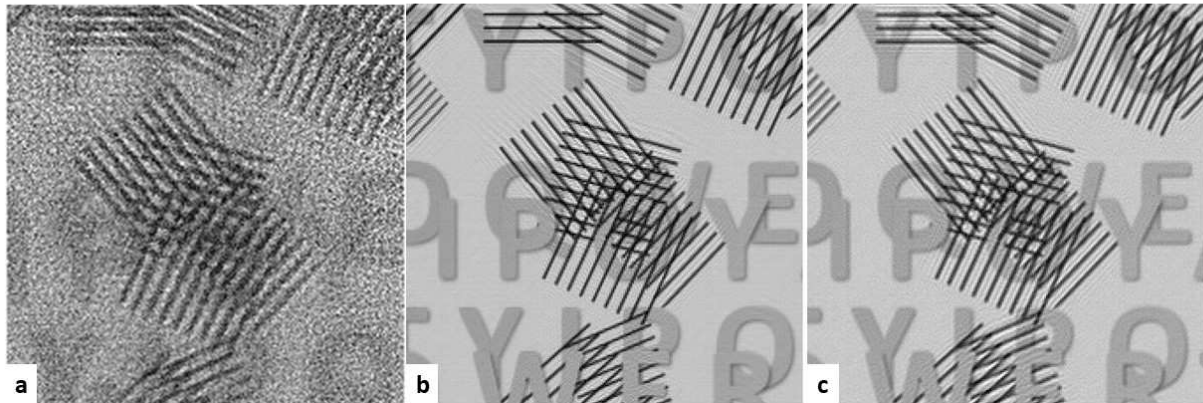


Fig. 10 shows the reconstructions from the data shown in Fig. 8.b. (a) shows the reconstruction with the conventional ePIE; the reconstruction is very noisy; the fringes are blurred, and the letters in the background have nearly disappeared. (b) shows the reconstruction with the extra mode method; (c) shows the reconstruction with the pedestal matching method. Both the two methods have improved the reconstruction quality a lot.

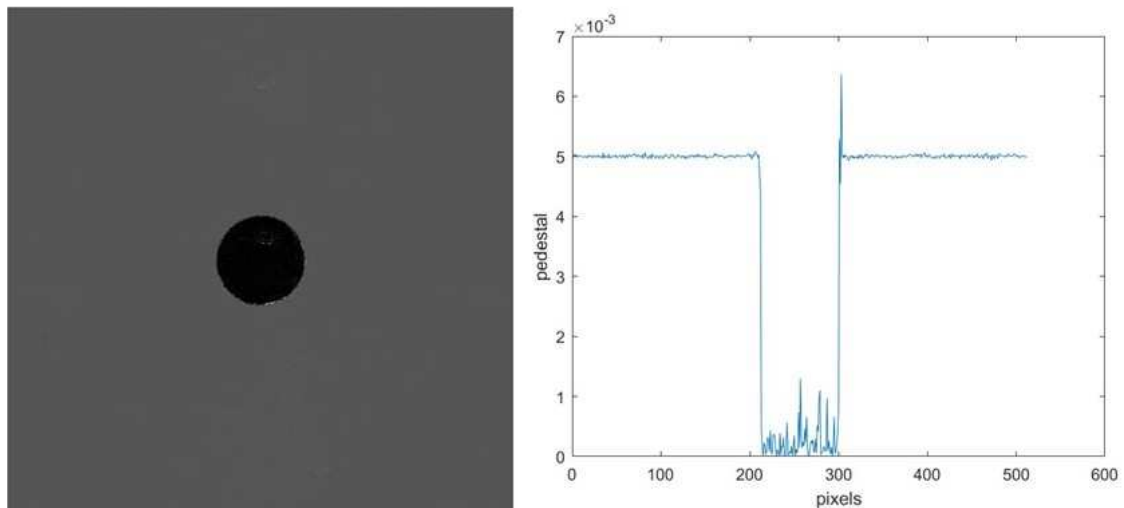


Fig. 11 shows the retrieved detector pedestal at one position with the extra mode method; the right image plots the retrieved values of the pedestal; the values outside the central disk area are about 0.005, which

have been retrieved accurately; the values inside the central disk area are nearly 0; which failed to be retrieved by the algorithm.

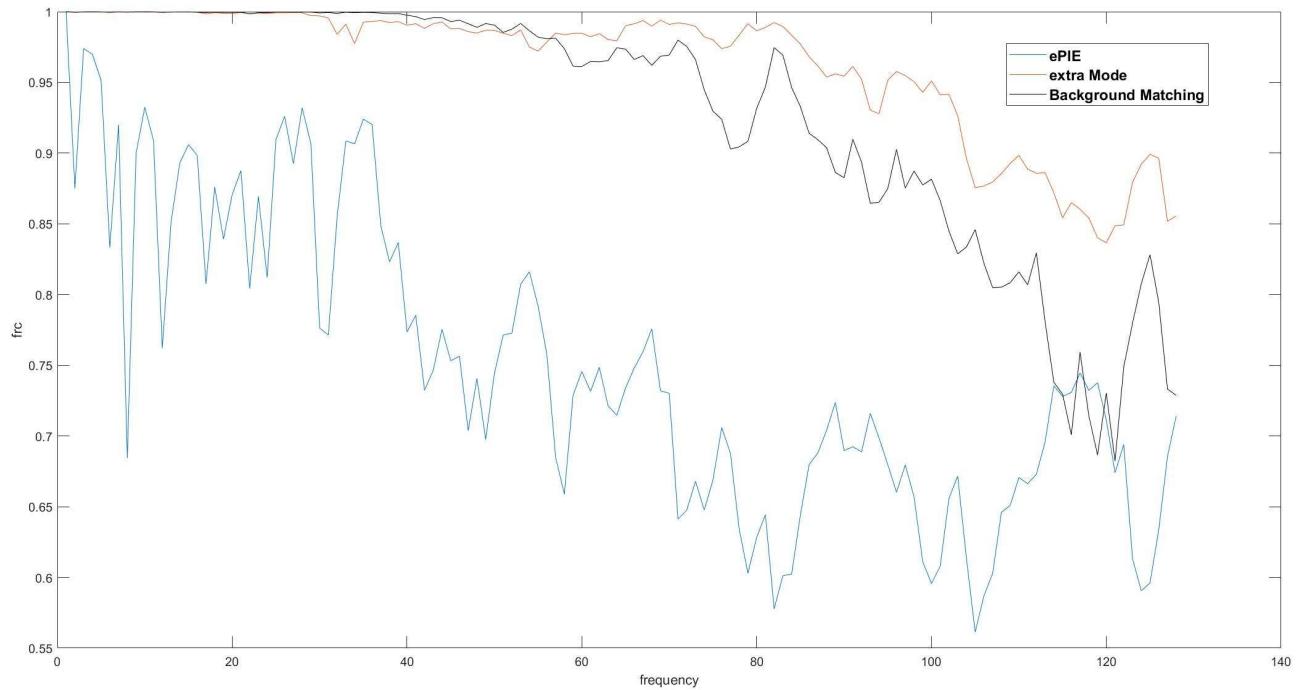


Fig. 12 plots the Fourier Ring Correlation of the reconstruction on the detector pedestal data. The blue line plots the FRC between the true object with the ePIE reconstruction; the red line plots the FRC between the true object with the extra mode reconstruction; the black line plots the FRC between the true object with the background matching reconstruction.

2.4 Data truncation

The experimental electron data that we will process in Section 3 was not saved as the full detector size because of limitations of computer memory. When the data is truncated artificially, some of the high-frequency information on the diffraction pattern will be lost. As the red dash lines show in Fig. 9.a, when the data was truncated as $\frac{3}{4}$ or $\frac{1}{2}$ of the original size, some speckles at the edge part will be lost. Since these speckles define the location of the high-frequency fringes in the crystallites, we suspect that the truncated diffraction patterns may be another cause of feature delocalization.

Fig. 14.a shows the ePIE reconstruction from the half-truncated data: it is obvious that there are some artificial fringes lying outside the boundaries and that the features have lost resolution.

The method we applied to improve the reconstruction of the truncated data is called super-resolution, which is a method that reconstructs beyond the diffraction limit resolution by extending the frame dimension of the diffraction patterns [31 - 34]. We can extend the frame size of the diffraction patterns in ptychographic reconstruction because of the redundancy in the dataset [33]. In this simulation, we put the truncated data into a box with a larger size as shown in Fig. 13: the 256*256 diffraction pattern was put in a 512*512 box. We use the extended diffraction patterns to do the reconstruction with ePIE. In the update with the Fourier domain constraint, we replace the modulus of the calculated intensities inside the original frame size area with the detected intensities I , while in the extended area, we leave the same as the calculation. This is the equation for the Fourier domain constraint update with the super-resolution method:

$$\Psi'_j = M \cdot \sqrt{I} \frac{\Psi_j}{\sqrt{\sum_j |\Psi_j|^2}} + (1 - M) \cdot |\Psi_j| \frac{\Psi_j}{\sqrt{\sum_j |\Psi_j|^2}}, \quad (15)$$

where M is a 1-0 filter, the pass area of which is the original diffraction pattern area.

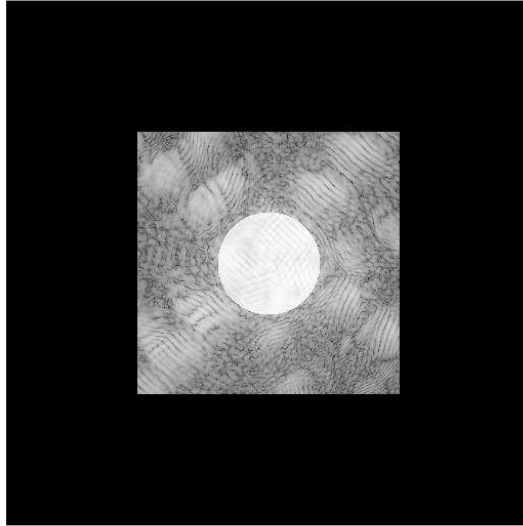


Fig. 13 shows an example of the $\frac{1}{2}$ truncated diffraction pattern when embedding in a 512×512 box for the super-resolution reconstruction.

The reconstruction from the $\frac{1}{2}$ truncated dataset with the super-resolution method is shown in Fig. 14.b. Compared with the result without extending the frame size in Fig. 14.a, most of the artificial fringes have disappeared, and the features are sharp, i.e. the resolution has been improved. However, there are still some slight fringes outside the boundaries. Estimating whether or not experimental data needs an extended frame size can be determined by observing the levels of intensity right at the edge of the detector frame: if this is high relative to the noise floor then we can infer that some scattered radiation has fallen outside the detector and hence should be reconstructed via the super-resolution method.

In conclusion, data truncation results in both features delocalization and resolution loss in the ptychographic reconstruction. The super-resolution method can improve the reconstruction because of the information redundancy in the dataset. However, there is a limit on the extent of the truncated area for the super-resolution method that depends on the overlap in real space, the illumination and the sample structure. The collection angle, which is decided by the camera length and the detector dimension, determines the reconstruction resolution. Usually, when the collection angle satisfies the aimed resolution, there is no necessary to

apply super-resolution in the reconstruction. However, in the case of the experimental data demonstrated in this paper (Fig. 18), it is obvious that some high-angle scattering speckles were partially cut off, so super-resolution method should be applied to retrieve the high-resolution information, which is related to these high-angle scattering speckles.

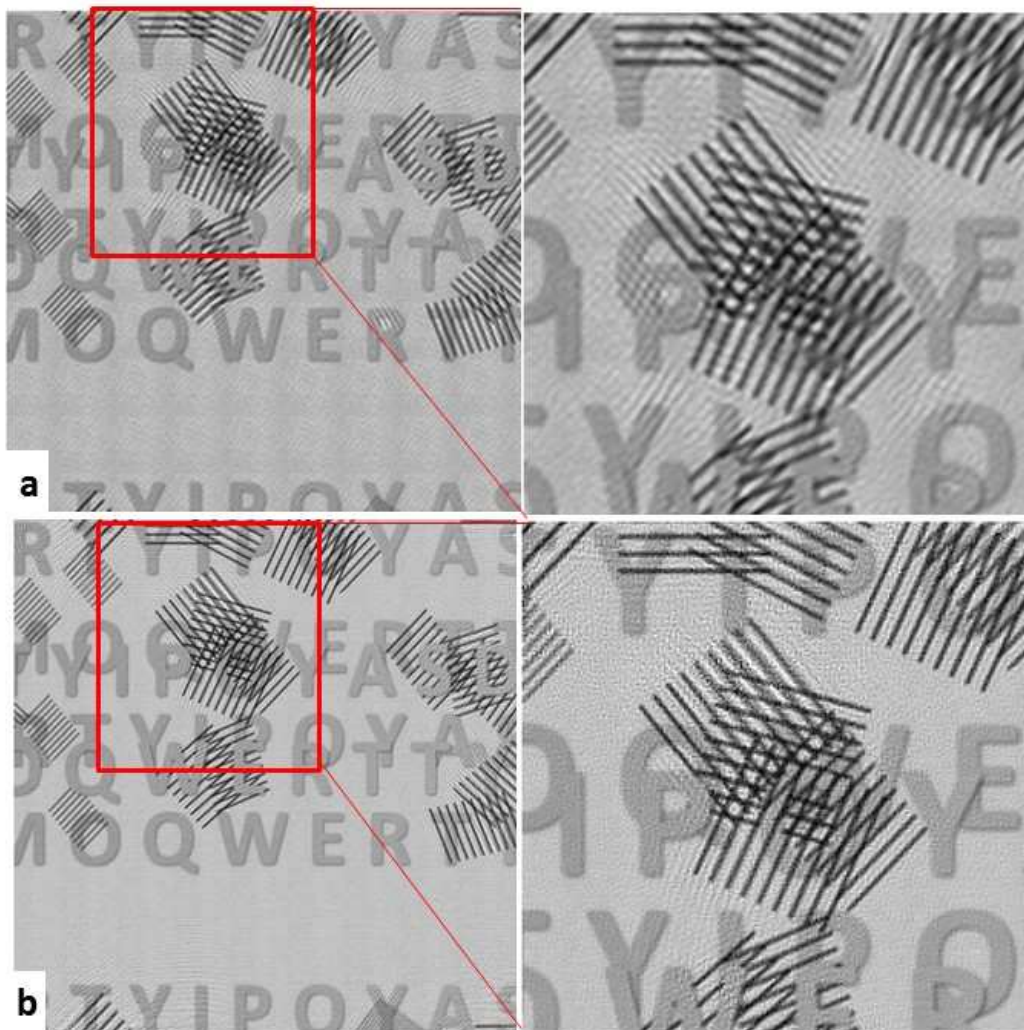


Fig. 14 shows the reconstructions from the $\frac{1}{2}$ truncated dataset. (a) shows the result with the conventional ePIE; the resolution of the features is low, and there are some artificial fringes. (b) shows the reconstruction with the super-resolution method; the features are sharper and most of the artificial fringes disappeared except that, there are still some slight fringes at the boundaries area.

2.5 Probe position scaling error: the ‘defocus-position coupling’ effect

The accuracy of the scanning positions is a critical factor that decides the quality of ptychographic reconstruction [35 - 38]. We can divide the scanning position errors into two categories: random positions errors and global errors such as scaling and rotation. Several methods which work efficiently to correct the random positions errors have been proposed, for example, the annealing method [37], and the exit wave cross-correlation method [38]. Global position errors are introduced when there is an error in the calibration of the shifting pitch of the sample stage or the illumination. In this section, we investigate the effect of a global scaling error on ptychographic reconstruction [39].

We reconstructed a set of ptychographic data with the scanning positions scaled by 1%, 3% and 10% respectively. Fig. 15 plots the scaled position maps. Fig. 16 shows the reconstructions of the sample from the scaled positions with ePIE as well as the annealing method. We can see that when there is 1% global scaling on the positions, the reconstruction loses resolution slightly; when the error is 3% and 10%, the reconstructed object looks out of focus: the features are blurred and delocalized. The annealing algorithm could not recover the correct positions.

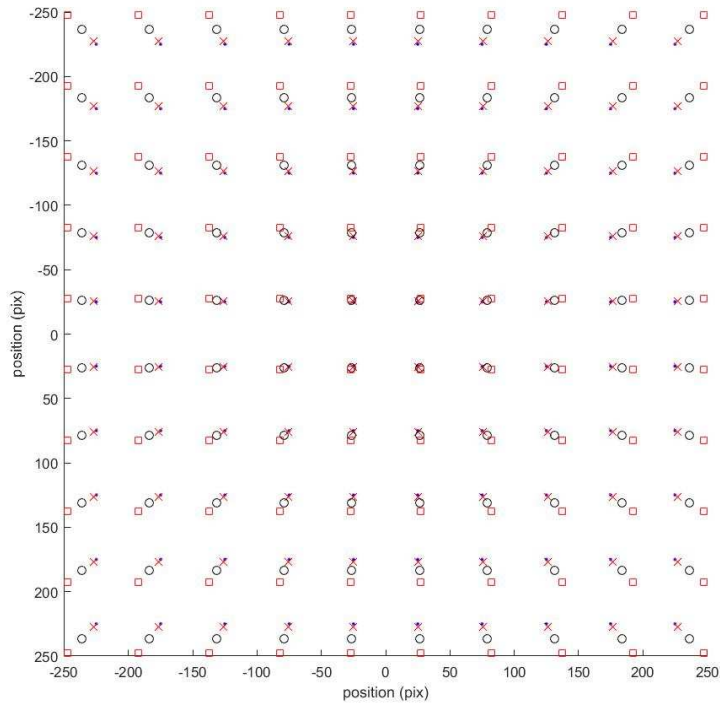


Fig. 15 shows the scaled scanning positions. The black dots show the accurate positions; the red crosses show the positions when stretched by 1%; the black circles show the positions when stretched by 3%; the red squares show the positions when stretched by 10%.

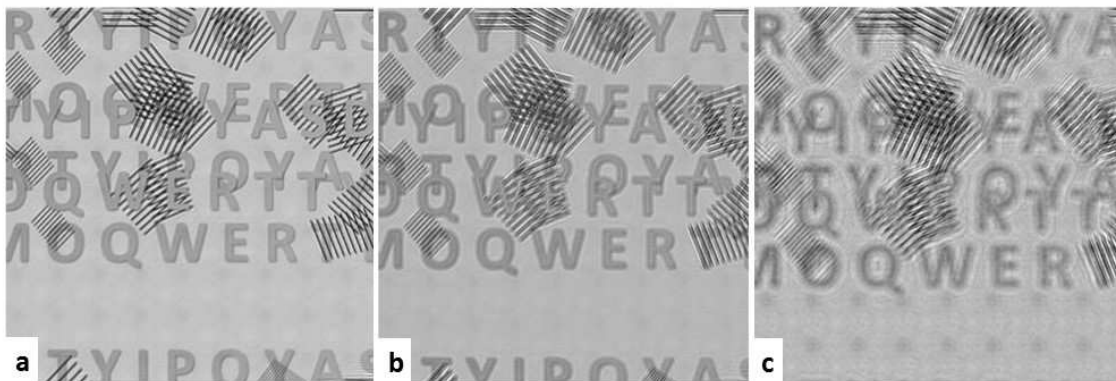


Fig. 16 shows the reconstructions of the sample with the scaled positions. (a) shows the reconstruction when the positions are stretched by 1%; the features of the sample lost the resolution slightly. (b) shows the reconstruction when the positions are stretched by 3%; the features are significantly blurred. (c) shows the reconstruction when the positions are stretched by 10%; it appears like an out of focus image.

This ‘defocus-position coupling’ reconstruction phenomenon can be qualitatively explained via Fig. 17. Convergent incident waves come from the left-hand side of the diagram.

Consider first a simple ray optics approximation. The real specimen (labeled ‘specimen’) lies some distance to the left of the beam focus. In the lower diagram, the specimen has been moved upwards by the distance shown by the large solid pointer. A feature in the specimen is seen to move across the Ronchigram in the far-field. However, there could exist a ‘pseudo specimen’, closer to the beam cross-over, which moves by a much smaller distance (denoted by the small solid pointer), which has a correspondingly small illumination function, yet creates the same effect (feature movement) on the far-field detector. Indeed, in the world of ray optics, it is completely impossible to tell the difference between the specimen and the pseudo specimen if we do not know how far we have moved the specimen.

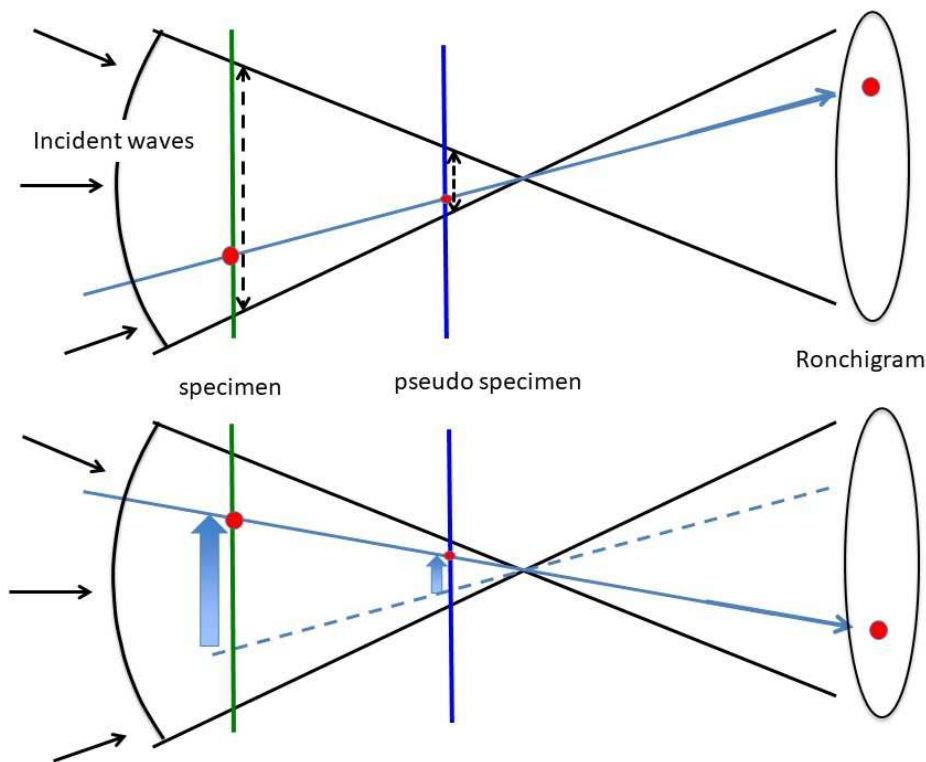


Fig. 17 illustrates the ‘defocus-position coupling’ reconstruction phenomenon. When the wave property of the electron wave is not considered, inside the central disc of the Ronchigram is a shadow image of the illuminated area. Thus, the structure inside the central disc is possible to correspond to any defocused planes with a suitable scaling factor.

Of course, when the wavelength of the radiation is large relative to the scale of this experiment, the Ronchigram is full of interference effects, reminiscent of Fresnel fringes, like those shown in Fig. 4. There are two consequences. First, when the step size of the illumination is wrongly calibrated, the reconstruction algorithm is forced to shrink (or expand) the scale of the image (and the illumination) to make it fit the main features of the Ronchigram, but the Ronchigram itself has Fresnel effects scaled according to the real defocus of the convergent probe. This conflicting information generates a seemingly out of focus, wrongly scaled reconstruction, which bears no relationship to any actual wave disturbance within the experiment: attempting to propagate this out of focus reconstruction will never put it into focus. Secondly, if we are trying to solve for the probe scan distortion, the algorithm can only rely on the Fresnel fringes to steer it to the correct solution. If there is any partial coherence in the beam, these fringes are weak and washed out, making the solution space highly ambiguous.

In conclusion, the global scaling error of the scanning positions will make the reconstructed sample look like an out of focus image; image features will be blurred and there will be no clear boundaries. Correcting a global scaling error in the probe positions in the defocused geometry is very difficult.

Once again we remark that X-ray defocused probe ptychography does not suffer from this problem because the stage step size and the precise defocus of the probe can be accurately calibrated. We also remark that any error in the camera length (the effective distance from the object to the detector) has the same effect as wrongly calibrating the probe step size. For this reason, defocused probe ptychography in the TEM is also difficult because once the lens settings are changed from imaging mode to diffraction mode, the effects of hysteresis mean the camera length is rarely calibrated to better than 2-5%: easily enough to wreck a reconstruction.

3 Refinement of experimental data

In this section, we reprocess the data obtained by Humphry et.al. [19] using the improvements we have modeled: modal decomposition to remove partial coherence, removal of the detector point spread effect, correction of the detector pedestal and detector data truncation. We also investigate how the experimental image is affected by position stretch, but find that the experimentally calibrated values of the magnification of the microscope (which defines the probe position stretch) and the accurately measured camera length does indeed give the best reconstruction.

The data were collected on an FEI Quanta 600 SEM with a thermally assisted Schottky field emission gun accelerated at 30 KeV [19]. The experimental setup can be simplified as Fig. 3: the condenser system formed a defocused probe with a diameter about 15nm on the sample, which was gold particles on holey carbon film; a CCD detector was placed in the far field (at a distance about 0.127m), with a dimension of 2048*2048 pixels and each pixel 7.4um. The detector was binned by 2 to collect the diffraction patterns, so the frame size of the diffraction patterns is 1024*1024, which is truncated as 768*768 for saving the data because of limited computer memory. 20*20 diffraction patterns were collected by shifting the illumination with a step size about 5nm. Fig. 18 shows one of the diffraction patterns, which was truncated as 768*768 and embedded in a 1024*1024 box.

For the modal decomposition on this experimental data, we used 16 probe functions and one object function. 30 iterations of ePIE were run first to give the initial object function and probe function; then 16 probes were generated from the ePIE reconstructed probe, to continue the 800 iterations modal decomposition reconstruction. To retrieve the detector pedestal, we applied the extra mode method. Fig. 21 shows an example of the retrieved detector pedestal at one scan position. Fig. 20 shows the first eight modes of the partially

coherent illumination arising from the effect of the detector point spread function. The modes were propagated to the condenser aperture.

From the above, we can conclude that this experiment was rather incoherent, and that this may be the main source of delocalization in the original reconstruction. The detector also had a significant pedestal. Fig. 21 shows interesting structure. Phosphors tend to saturate under very strong illumination (as we find in the Ronchigram central disc) and can have significant afterglow effects. This may account for the overall offset within the central disk. We can speculate that the halo around the central disk is due to small angle inelastic scattering, which will not correlate strongly with the specimen structure, and so would come out in the extra 'free mode' method we employ. Further investigation is needed to clarify the performance of this free mode technique, however, before we can definitively relate Fig. 21 to physical aspects of the experiment itself, and discount algorithmic artifacts as a cause.

Finally we observe that the final reconstruction (Fig.19), when taking into account all these effects, is somewhat better than the previously published result by Humphry et. al.: the contrast of the carbon film is better, and the gold fringes are certainly more localized.

The result shown in Fig.19 has used the experimentally measured camera length and microscope magnification calibration, which determines the overall probe position scaling. In Fig.22 we test the effect stretching the estimated probe positions by +/-1% and +/-3%. As expected, even this tiny error seriously affects the fringe locations. The contrast of the reconstruction also gets lower when the positions have a scaling error. It is reasonable to suppose that the contrast reaches a maximum only when the Fourier components of the image are exactly correct. This also implies that the calibration of the original experiment was indeed accurate to within 1%.

The semi convergence angle of the experimental setup was 6 mrad, which at this accelerating voltage implies a diffraction-limited resolution of approximately 1nm. The nominal resolution of the instrument is 1.2nm. In our reconstruction the 0.236nm gold atomic fringes are very clearly visible; clear evidence of the resolution improvement obtained by ptychography. Interestingly, we can use the modal decomposition method to reconstruct the intensity of the source profile. This is achieved by back-propagating each mode to the source plane and adding the intensity of all the modes together. The result is shown in Figure 2.3. It should be emphasised that this is not the physical distribution of the source, but its apparent distribution as seen backwards up the column ‘through’ the condenser lens. Or, equivalently, the source profile convolved with impulse response of the microscope. The FWHM of this function is 1.7nm: rather larger we might expect. However, the fact that less than 20% of the source flux falls within the first mode (Fig. 20) compared to 47% for our modelled data corroborates this result. The coherence of the experimental data is indeed quite low.

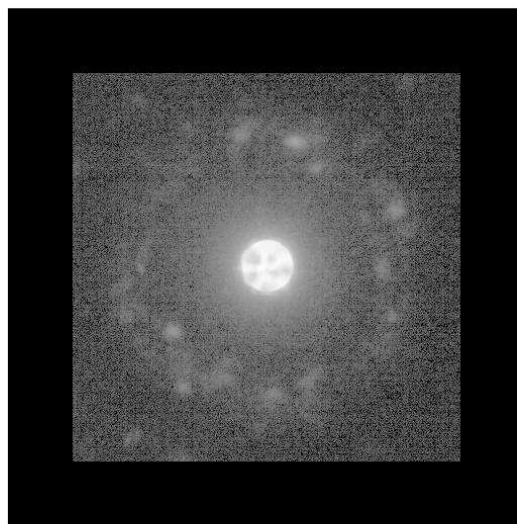


Fig. 18 shows one diffraction pattern of the experimental data, which is plotted in logarithm scale; the data was truncated as 768*768; in the super-resolution reconstruction, the truncated data is embedded in the frame size of 1024*1024.

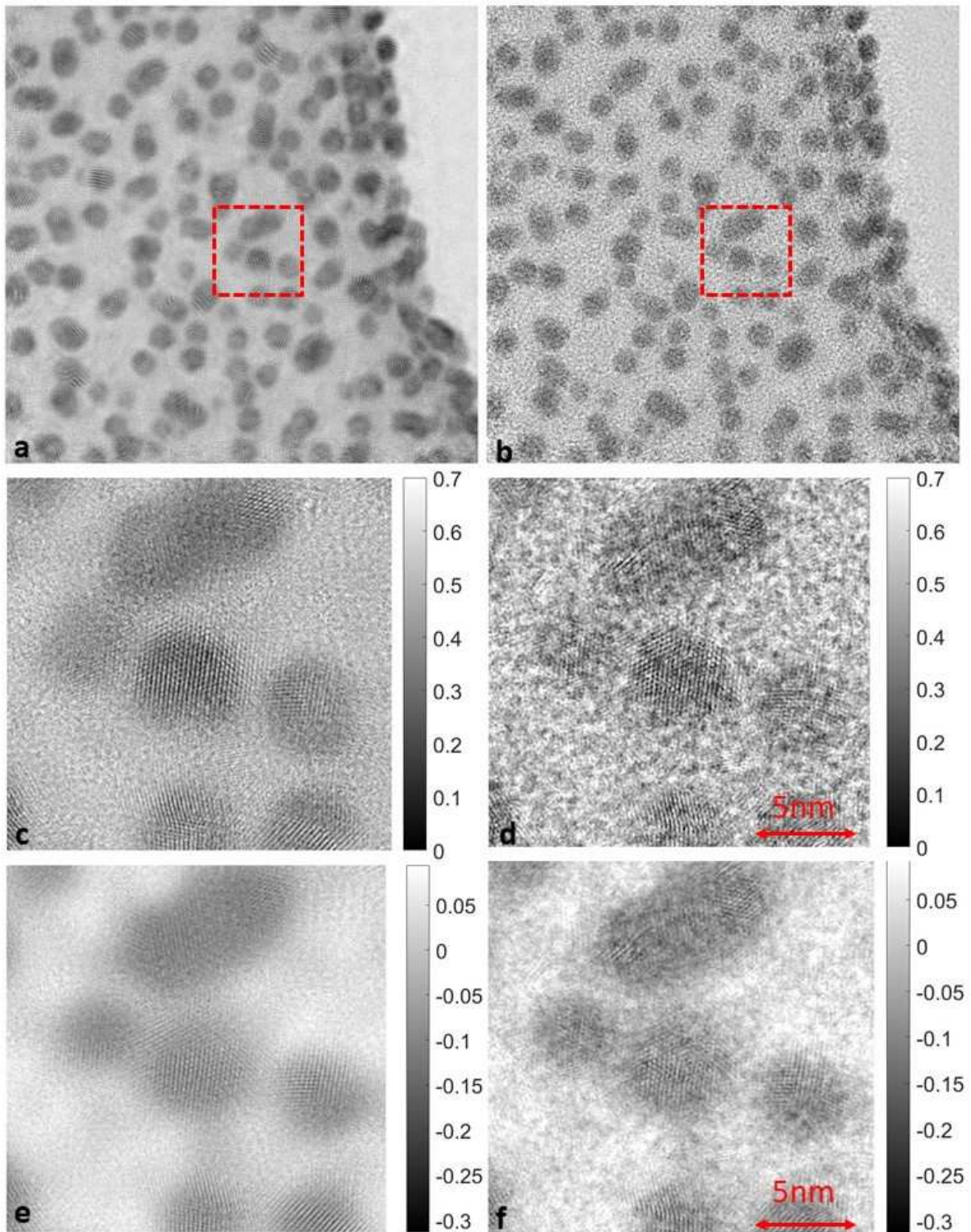


Fig. 19 compares the reconstruction result from the improved algorithm with the previously published result. (a) shows the whole reconstructed field of view with ePIE. (b) shows the whole reconstructed field of view with the improved algorithm. (c) and (e) show the modulus and phase of the dashed area in (a); (d) and (f) show the modulus and phase of the dashed area in (b).

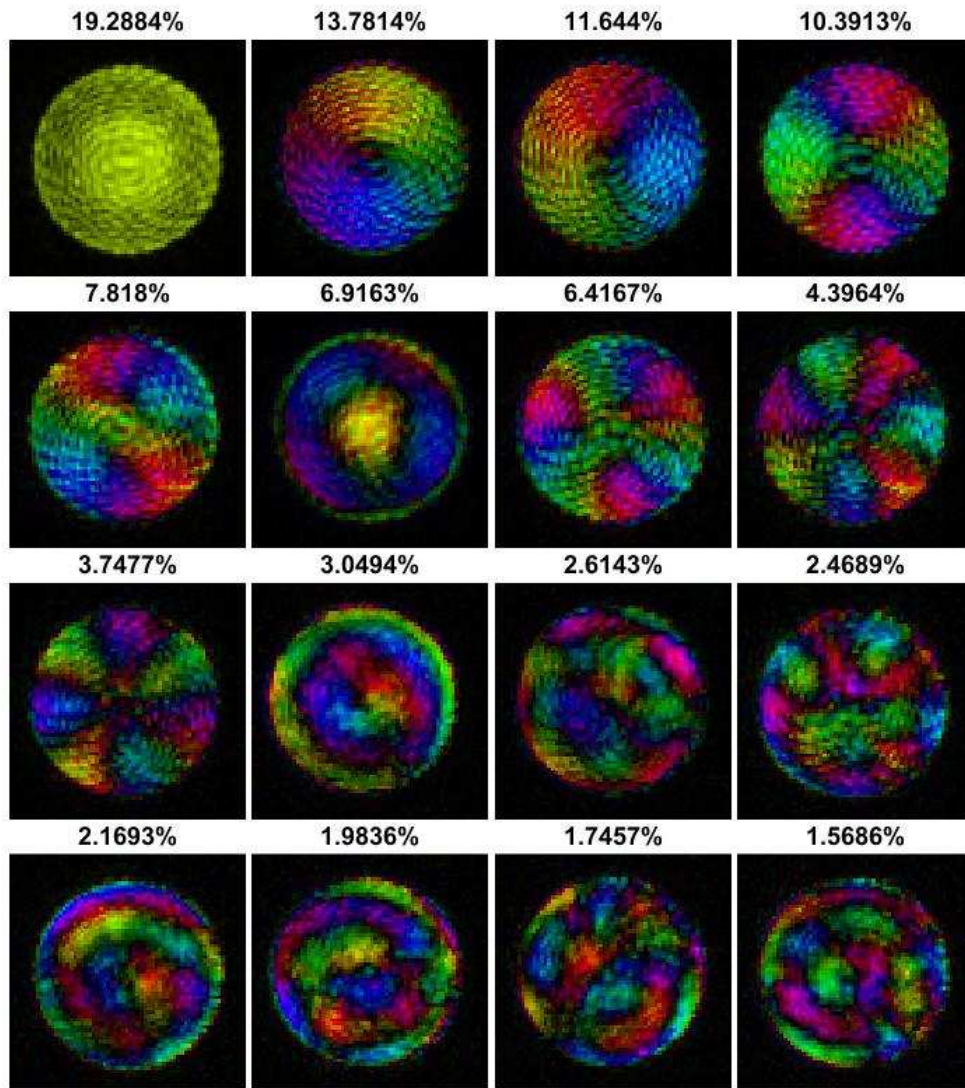


Fig. 20 shows the retrieved modes of the effective electron source with the modal decomposition method; the modes were presented at the condenser aperture plane. These modes include the effect of both the source transverse partial coherence and the detector point spread. The fringe structure arises from the shape edge of the truncated data when fitted into a larger box for the super-resolution method.

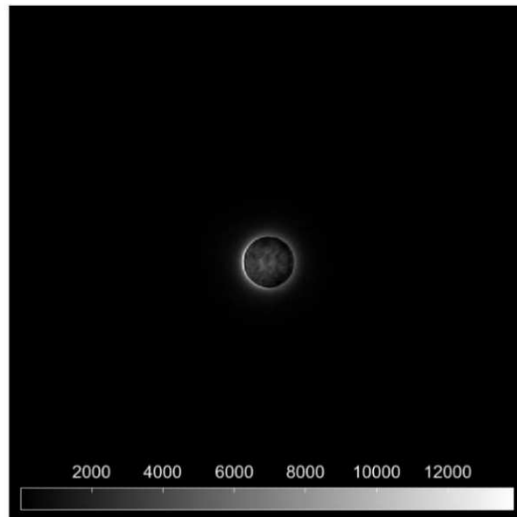


Fig. 21 shows the retrieved detector pedestal at one scanning position from the experimental data with the extra mode method.

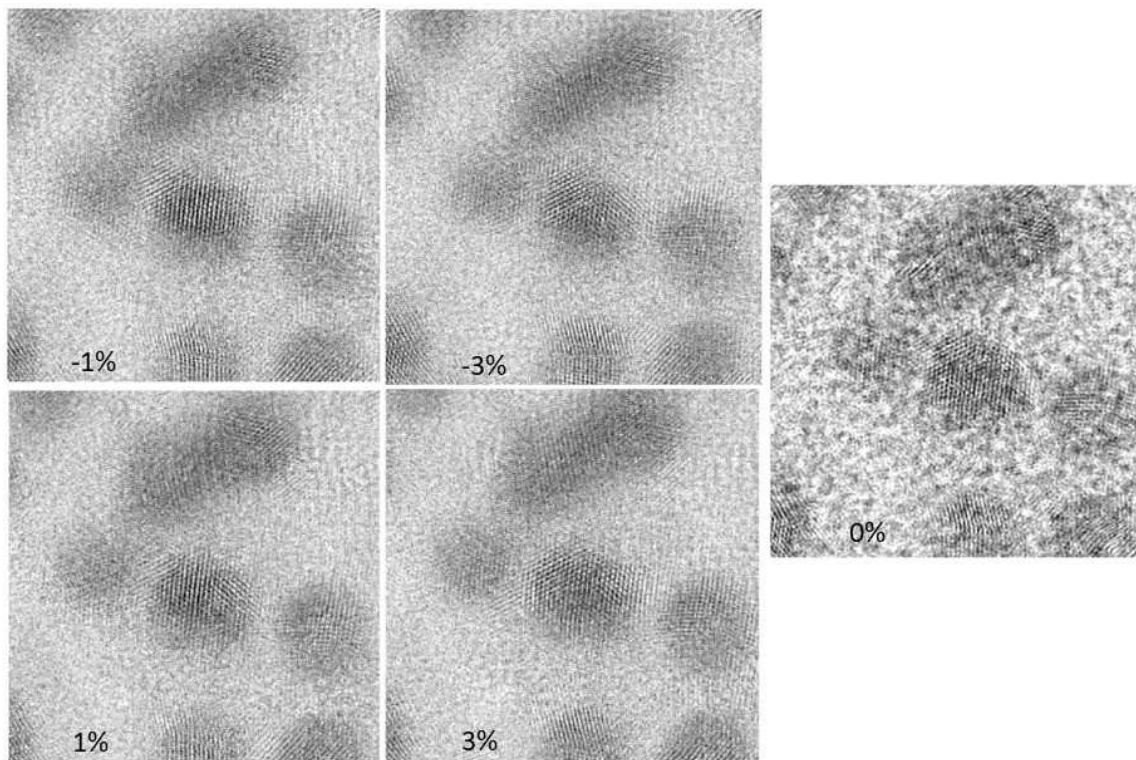


Fig.22 shows the specimen reconstructions when there is a 1% and 3% global stretching or compression (-) of the probe positions. When there is 1% stretching/squashing, the fringes ready appear delocalized, and the contrast gets lower. When the stretching/squashing arrives at 3%, the delocalization issue gets worse.

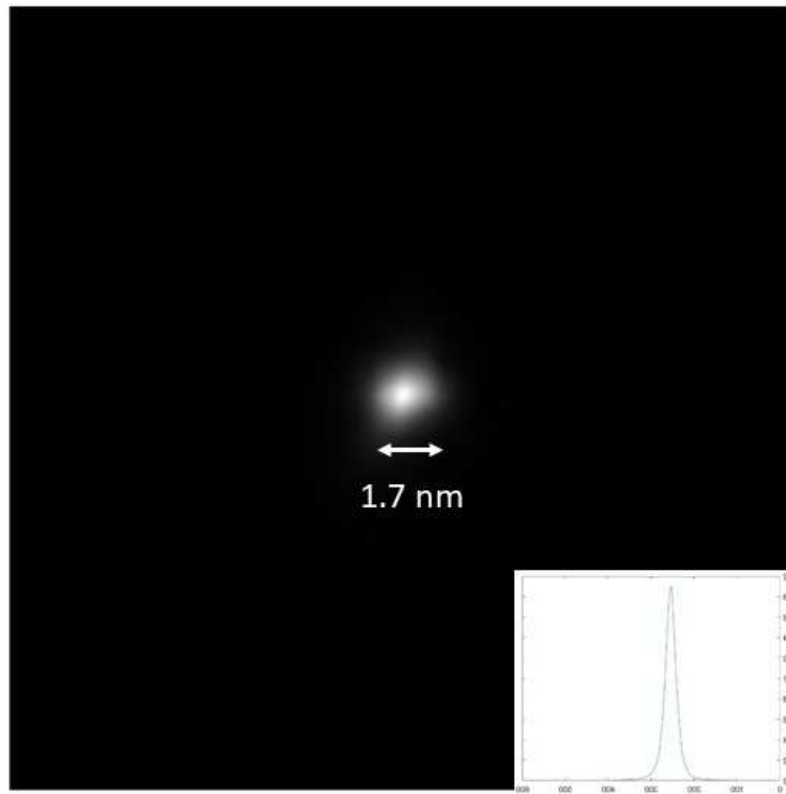


Fig. 23 shows the reconstructed effective source profile of the SEM, which equals the actually demagnified electron source convolved with the condenser aperture. The effective source profile has a width of about 1.7 nm at the half maximum.

4 Conclusion

In this paper, we have attempted to diagnose the delocalization problem existing in previously published defocused probe SEM ptychography reconstruction that used the conventional ePIE algorithm. We found out that the partial coherence of the source, the detector point spread, the detector response pedestal, data truncation, and a global error in the scanning positions all result in delocalization effects and loss of resolution at one level or another.

The scanning positions are the key factor that decides the resolution of the specimen reconstruction. Even a slight global scaling error in the scanning positions will result in the reconstructed object appearing out of focus. The transverse partial coherence of the source, as

well as the effect of the detector point spread, is the second factor that affects the quality of the reconstruction. Both of them result in degraded contrast, causing object features to become blurred, and atomic fringes to be delocalized. The modal decomposition method works efficiently to remove the effects of source partial coherence and the effect of detector point spread.

The next factor that affects the reconstruction quality is the detector background read-out noise pedestal. A reconstruction from a dataset with a significant background pedestal will be very noisy, with some features completely disappearing. There are several methods to reduce the effect of the detector pedestal before the processing, for example, removing a reference from each diffraction patterns when collecting the data, or taking off a constant pedestal from the whole dataset manually. However, even though these methods do improve the reconstruction quality significantly, they are still not accurate enough, because the pedestal may vary between different pixels and it may change nonlinearly according to the counts of the electrons or photons. It is also possible to retrieve the pedestal from the reconstruction, thanks to the rich redundancy in the ptychographic dataset. Two efficient methods, pedestal matching, and using an extra ‘free mode’ have been proposed: here we applied the extra mode method to reconstruct the pedestal. Another factor that results in the delocalization in the Humphry et. al. paper [19] is data truncation. Our work shows that this will also result in some artificial fringes in the reconstruction and the loss of resolution.

We reprocessed the Humphry et. al. data [19] with the ePIE algorithm, improved with the modal decomposition method, super-resolution, and extra modes for handling faults in the detector. The resulting reconstruction has certainly been improved over the original work, with better phase contrast of the light atoms (the carbon film), and better localization of the atomic gold fringes within the gold nanoparticles. Our improved algorithm relaxes the demand on the experiment parameters, such as the illumination coherence and the properties

of the detector. It must be said, though, that solving for so many experimental errors retrospectively should be avoided if at all possible. Convergence properties of iterative algorithms are hard, if not impossible, to prove for the simplest systems. When so many variables are included in a single inverse calculation, any uncertainty in the result becomes impossible to bracket.

What does all this tell us about electron ptychography in the SEM? Is it a technique worth pursuing? Unlike the dense real space sampling methods (WDD deconvolution, and its weak object counterpart [4], the defocused method does not obtain its resolution performance from a good lens. SEM's do not generally have aberration correctors, so the vision of an inexpensive 'TEM in a SEM' can most easily be achieved using the defocused configuration. But, as we have seen, this has many experimental hazards, which also seriously impact the reconstruction process. Results would certainly be much improved if we were able to use a single electron counting detector, electrostatic scan coils (which will move the probe much more reliably) and a cold field emission gun. However, except for electrostatic scanning, these modifications are so expensive, at least at the time of writing, that the idea of a low-cost, high-performance TEM in a SEM is somewhat negated. Furthermore, working at low keV will always confine the technique to rather thin specimens (perhaps only single atomic layers). Nevertheless, it is possible that a more global approach to the inversion problem, taking into account all the lessons we have learned, will eventually deliver absolutely reliable high-resolution electron ptychographic reconstructions from an inexpensive setup.

Acknowledgements

S. Cao is grateful for a Ph.D. studentship funded by Phase Focus Ltd to undertake this work, and for further funding by the Department of Electronic and Electrical Engineering at the University of Sheffield.

References

- [1] O. Bunk, M. Dierolf, S. Kynde, I. Johnson, O. Marti and F. Pfeiffer, "Influence of the overlap parameter on the convergence of the ptychographical iterative engine," *Ultramicroscopy*, vol. 108, p. 481, 2008.
- [2] R.H.T. Bates and J.M. Rodenburg, "Sub-Angstrom Transmission Microscopy: a Fourier Transform Algorithm for Microdiffraction Plane Intensity Information," *Ultramicroscopy*, vol. 31, pp. 303-308, 1989.
- [3] J.M. Rodenburg and R.H.T. Bates, "The theory of super-resolution electron microscopy via Wigner-distribution deconvolution," *Phil. Trans. R. Soc. Lond. A*, vol. 339, pp. 521-553, 1992.
- [4] J.M. Rodenburg, B.C. McCallum and P.D. Nellist, "Experimental Tests on Double Resolution Coherent Imaging via STEM," *Ultramicroscopy*, vol. 48, pp. 304-314, 1993.
- [5] P. D. Nellist, B. C. McCallum and J. M. Rodenburg, "Resolution beyond the 'information limit' in transmission electron microscopy," *Nature*, vol. 374, p. 630, 1995.
- [6] W. Hoppe, "Diffraction in inhomogeneous primary wave fields. 1. principle of phase determination from electron diffraction interference," *Acta Crystallographica Section A - Crystal Physics Diffraction Theoretical and General Crystallography*, vol. A 25, p. 495, 1969.
- [7] R. Hegerl and W. Hoppe, "Dynamic theory of crystalline structure analysis by electron diffraction in inhomogeneous primary wave field," *Berichte der Bunsen-Gesellschaft Fur Physikalische Chemie*, vol. 74, p. 1148, 1970.
- [8] T. J. Pennycook, A.R. Lupini, H. Yang, M.F. Murfitt, L. Jones and P. D. Nellist, "Efficient phase contrast imaging in STEM using a pixelated detector. Part I: Experimental demonstration at atomic resolution," *Ultramicroscopy*, vol. 151, pp. 160-167, 2015.
- [9] H. Yang, P. Ercius, P. Nellist and C. Ophus, "Enhanced phase contrast transfer using ptychography combined with a pre-specimen phase plate in a scanning transmission electron microscope," *Ultramicroscopy*, vol. 171, p. 117, 2016.
- [10] H. Yang, R.N. Rutte, L. Jones, M. Simon, R. Sagawa, H. Ryll, M. Huth, T.J. Pennycook, M.L.H. Green, H. Soltau, Y. Kondo, B.G. Davis and P.D. Nellist, "Simultaneous atomic-

- resolution electron ptychography and Z-contrast imaging of light and heavy elements in complex nanostructures,” *Nat. Commun.*, vol. 12532, p. 1, 2016.
- [11] H. Yang, I. MacLaren, L. Jones, G. Martinez, M. Simson, M. Huth, H. Ryll, H. Soltau, R. Sagawa, Y. Kondo, C. Ophus, P. Ercius, L. Jin, A. Kovacs and P. Nellist, “Electron ptychographic phase imaging of light elements in crystalline materials using Wigner distribution deconvolution,” *Ultramicroscopy*, vol. 180, pp. 173-179, 2017.
- [12] P. Thibault, M. Guizar-Sicairos and A. Menzel, “Coherent imaging at the diffraction limit,” *Journal of Synchrotron Radiation*, vol. 21, pp. 1011-1018, 2014.
- [13] H.M.L. Faulkner and J.M. Rodenburg, “Movable aperture lensless transmission microscopy: a novel phase retrieval algorithm,” *Phys. Rev. Lett.*, vol. 93, p. 023903-1, 2004.
- [14] J.M. Rodenburg and H.M.L. Faulkner, “A phase retrieval algorithm for shifting illumination,” *Applied Physics Letters*, vol. 85, p. 4795, 2004.
- [15] P. Thibault, M. Dierolf, A. Menzel, O. Bun, C. David and F. Pfeiffer, “High-resolution scanning X-Ray diffraction microscopy,” *Science*, vol. 321, p. 379, 2008.
- [16] P. Thibault, M. Dierolf, O. Bunk, A. Menzel and F. Pfeiffer, “Probe retrieval in ptychographic coherent diffractive imaging,” *Ultramicroscopy*, vol. 109, p. 338, 2009.
- [17] A. M. Maiden and J. M. Rodenburg, “An improved ptychographical phase retrieval algorithm,” *Ultramicroscopy*, vol. 109, p. 1256, 2009.
- [18] P. Thibault and A. Menzel, “Reconstructing state mixtures from diffraction measurements,” *Nature*, vol. 494, p. 68, 2013.
- [19] M.J. Humphry, B. Kraus, A.C. Hurst, A.M. Maiden and J.M. Rodenburg, “Ptychographic electron microscopy using high-angle dark-field scattering for sub-nanometre resolution imaging,” *Nature Comms*, vol. 1733, p. 1, 2012.
- [20] J.M. Rodenburg, A.C. Hurst, A.G. Cullis, B.R. Dobson, F. Pfeiffer, O. Bunk, C. David, K. Jefimovs and I. Johnson, “Hard-X-Ray lensless imaging of extended objects,” *Phys. Rev. Lett.*, vol. 98, pp. 034801-1, 2007.
- [21] D.T. Nguyen, S.D. Findlay, J. Etheridge, “The spatial coherence function in scanning transmission electron microscopy and spectroscopy,” *Ultramicroscopy*, vol. 146, pp. 6-16, 2014.
- [22] A.M. Maiden, M.C. Sarahan, M.D. Stagg, S.M. Schramm and M.J. Humphry, “Quantitative electron phase imaging with high sensitivity and an unlimited field of view,” *Scientific Reports*, vol. 5, p. 1, 2015.
- [23] N. Burdet, X. Shi, D. Parks, J. N. Clark, X. Huang, S. D. Kevan and I. K. Robinson, “Evaluation of partial coherence correction in X-ray ptychography,” *Opt. Express*, vol. 23, p. 5452, 2015.
- [24] C. Maunders, C. Dwyer, P.C. Tiemeijer and J. Etheridge, “Practical methods for the measurement of spatial coherence - A comparative study,” *Ultramicroscopy*, vol. 111, pp.

1437-1446, 2011.

- [25] S. Cao, P. Kok, P. Li, A.M. Maiden and J.M. Rodenburg, "Modal decomposition of a propagating matter wave via electron ptychography," *Phys. Rev. A*, vol. 94, pp. 063621-1, 2016.
- [26] E. Wolf, "New special representation of random sources and of the partially coherent fields that they generate," *Optics Communications*, vol. 38, p. 3, 1981.
- [27] M. Born and E. Wolf, *Principles of Optics*, Cambridge: Cambridge University Press, 1999.
- [28] P. Li, D.J. Batey, T.B. Edo, A.D. Parsons, C. Rau and J.M. Rodenburg, "Multiple mode x-ray ptychography using a lens and a fixed diffuser optic," *J. Opt.*, vol. 18, p. 1, 2016.
- [29] P. Li, T. Edo, D. Batey, J. M. Rodenburg and A. M. Maiden, "Breaking ambiguities in mixed state ptychography," *Opt. Exp.*, vol. 24, p. 9038, 2016.
- [30] S. Marchesini, A. Schirotzek, C. Yang, H. Wu and F. Maia, "Augmented projections for ptychographic imaging," *Inverse Problems*, vol. 29, p. 1, 2013.
- [31] R. Gerchberg, "Super-resolution through Error Energy Reduction," *Optica Acta*, vol. 21, pp. 709-720, 1974.
- [32] V. Mico, "Synthetic aperture superresolution with multiple off-axis holograms," *J. Opt. Soc. Am.*, vol. 23, p. 3162, 2006.
- [33] A.M. Maiden, M.J. Humphry, F. Zhang and J.M. Rodenburg, "Superresolution imaging via ptychography," *J. Opt. Soc. Am.*, vol. 28, p. 604, 2011.
- [34] J. Lindberg, "Mathematical concepts of optical superresolution," *J. Opt.*, vol. 14, p. 1, 2012.
- [35] H.M.L. Faulkner and J.M. Rodenburg, "Error tolerance of an iterative phase retrieval algorithm for moveable illumination microscopy," *Ultramicroscopy*, vol. 103, pp. 153-164, 2005.
- [36] F. Hue, J.M. Rodenburg, A.M. Maiden and P.A. Midgley, "Extended ptychography in the transmission electron microscope: Possibilities and limitations," *Ultramicroscopy*, vol. 111, pp. 1117-1123, 2011.
- [37] A.M. Maiden, M.J. Humphry, M.C. Sarahan, B. Kraus and J.M. Rodenburg "An annealing algorithm to correct positioning errors in ptychography," *Ultramicroscopy*, vol. 120, 2012.
- [38] F. Zhang, I. Peterson, J. Vila-Comamala, A. Diaz, F. Berenguer, R. Bean, B. Chen, A. Menzel, I.K. Robinson and J.M. Rodenburg, "Translation position determination in ptychographic coherent diffraction imaging," *Optics Express*, vol. 21, p. 13592, 2013.
- [39] S. Cao, P. Li, A.M. Maiden and J.M. Rodenburg, "Defocus and probe-position coupling in electron ptychography," in *European Microscopy Congress*, Lyon, 2016.

